nature communications

Article

https://doi.org/10.1038/s41467-025-56240-y

All-round enhancement induced by oxophilic single Ru and W atoms for alkaline hydrogen oxidation of tiny Pt nanoparticles

Received: 16 March 2024

Accepted: 13 January 2025

Wensheng Jiao[1,6], Zhanghao Ren[2,6], Zhibo Cui[1,6], Chao Ma[3,6], Ziang Shang[1], Guanzhen Chen[1], Ruihu Lu[2], Tao Gan[4], Ziyun Wang[2] ✉, Yu Xiong[5] & Yunhu Han[1] ✉

Anion exchange membrane fuel cells (AEMFCs) are one of the ideal energy conversion devices. However, platinum (Pt), as the benchmark catalyst for the hydrogen oxidation reaction (HOR) of AEMFCs anodes, still faces issues of insufficient performance and susceptibility to CO poisoning. Here, we report the Joule heating-assisted synthesis of a small sized Ru_1Pt single-atom alloy catalyst loaded on nitrogen-doped carbon modified with single W atoms (*s*-$Ru_1Pt@W_1/NC$), in which the near-range single Ru atoms on the Ru_1Pt nanoparticles and the long-range single W atoms on the support simultaneously modulate the electronic structure of the active Pt-site, enhancing alkaline HOR performance of *s*-$Ru_1Pt@W_1/NC$. The mass activity of s-$Ru_1Pt@W_1/NC$ is 7.54 A mg_{Pt+Ru}^{-1} and exhibits notable stability in 1000 ppm CO/H_2-saturated electrolyte. Surprisingly, it can operate stably in H_2-saturated electrolyte for 1000 h with only 24.60 % decay. Theoretical calculations demonstrate that the proximal single Ru atoms and the remote single W atoms synergistically optimize the electronic structure of the active Pt-site, improving the HOR activity and CO tolerance of the catalyst.

With the maturing of anion-exchange membranes and availability of inexpensive non-precious-metal catalysts as efficient cathodes, anion-exchange membrane fuel cells (AEMFCs) have awakened more and more interest in research and industry[1–4]. However, the anode, which is indispensable for AEMFCs, has failed to keep pace with the development, and still relies mainly on platinum (Pt)-based materials as catalysts for the hydrogen oxidation reaction (HOR)[5–7]. When the electrolyte changes from acidic to alkaline, the kinetics of anodic HOR becomes much slower, 2-3 orders of magnitude slower than in acidic media[8–10]. Therefore, to compensate for the loss of performance of AEMFCs due to slow kinetics, even the most advanced Pt-based catalysts still require a high Pt loading to achieve performance comparable to that of proton exchange membrane fuel cells (PEMFCs)[11,12]. In addition, Pt-based catalysts are extremely susceptible to poisoning by traces of carbon monoxide (CO, even <10 ppm) in the cheap crude hydrogen, leading to a drastic decrease in catalyst HOR performance[13,14]. Therefore, the exploration of alkaline HOR catalysts with high activity, stability and resistance to CO poisoning is significant for the development of AEMFCs.

Given the high cost and poor CO poisoning resistance of Pt-based catalysts, a great deal of effort has been put into the development of non-Pt-based catalysts with a view to replacing Pt-based catalysts[15,16]. However, contrary to expectations, the performance of non-Pt-based alkaline HOR catalysts is difficult to meet the requirements of industrialization[17,18]. This has forced researchers to turn the direction of the development of low-Pt alkaline HOR catalysts by seeking ways to

---

[1]Institute of Flexible Electronics (IFE), Northwestern Polytechnical University, Xi'an, China. [2]School of Chemical Sciences, The University of Auckland, Auckland, New Zealand. [3]Department of Chemistry, Tsinghua University, Beijing, China. [4]Shanghai Synchrotron Radiation Facility, Shanghai Advanced Research Institute, Chinese Academy of Sciences, Shanghai, China. [5]Chemistry and Chemical Engineering, Central South University, Changsha, China. [6]These authors contributed equally: Wensheng Jiao, Zhanghao Ren, Zhibo Cui, Chao Ma. ✉e-mail: ziyun.wang@auckland.ac.nz; iamyhhan@nwpu.edu.cn

reduce the usage of Pt while maintaining the intrinsic activity of the Pt active sites. According to the literature, reducing the size of Pt-based catalysts to clusters or single-atom dispersions is one of the very effective ways to reduce the amount of precious metal Pt usage and improve the alkaline HOR activity of the catalysts[19–22]. In addition, alloying Pt with oxygenophilic species to optimize the binding energy of *H and *OH (HBE and OHBE) by adjusting the surface oxidophilicity of the catalyst, which is beneficial to the improvement of the catalyst's alkaline HOR activity, is also a method that is well-established[23–25]. Recently, it has been reported that the coupling of the above two methods has achieved the enhancement of HOR activity and resistance to CO poisoning by using the long-range indirect action of the oxygenophilic metal single atoms on the active center[26]. This inspires us whether it is possible to achieve an all-round improvement in the comprehensive performance of the prepared catalyst alkaline HOR in terms of mass activity, stability and CO tolerance by cleverly designing the structure of the catalyst, such as introducing multiple oxophilic metals simultaneously, and by means of proximity direct optimization of the electronic structure of the active centers, as well as remote indirect optimization of the electronic structure of the active centers?

Herein, we report a bifunctional hydrogen electrocatalyst under alkaline solution prepared via Joule heating that consists of tiny Ru_1Pt single-atom alloy nanoparticles loaded on nitrogen-doped carbon modulated by W single atoms (s-$Ru_1Pt@W_1/NC$). s-$Ru_1Pt@W_1/NC$ possesses a great alkaline HOR performance, which is attributed to the regulated simultaneously electronic structure of tiny Pt nanoparticles by near-range single atoms Ru and long-range single atoms W. The lower Pt containing s-$Ru_1Pt@W_1/NC$ provides better HOR performance than commercial Pt/C and PtRu/C. The mass activity of 7.54 A mg_{PtRu}^{-1} is much larger than the 0.29 A mg_{Pt+Ru}^{-1} and 0.15 A mg_{Pt}^{-1} of commercial PtRu/C and Pt/C, respectively. Impressively, after operating 1000 h at 0.05 V vs. RHE in 0.10 M KOH, s-$Ru_1Pt@W_1/NC$ remains 75.40 % of its original current density, which is one of the most stable alkaline HOR catalysts achieved in testing at present on a gas diffusion electrode (GDE). More importantly, s-$Ru_1Pt@W_1/NC$ capability of the CO tolerance is also better than commercial Pt/C and PtRu/C. After 5000 s of operation at 0.10 V vs. RHE in the presence of 1000 ppm CO/H_2, s-$Ru_1Pt@W_1/NC$'s current dropped by 17.10 % of its initial current, while commercial Pt/C and PtRu/C are completely deactivated at 1850 s and 2780 s, respectively. Electrochemical tests and density functional theory (DFT) calculations demonstrate that the simultaneous introduction of proximal Ru single atoms and remote W single atoms with oxygenophilic properties modulates the electronic structure of the tiny Pt nanoparticles, optimizes the HBE and OHBE, weakens the adsorption of CO, and improves its ability to catalyze the conversion of CO to CO_2, which ultimately leads to the enhancement of the alkaline HOR performance.

Results

Synthesis and structural characterizations

s-$Ru_1Pt@W_1/NC$ was fabricated via the Joule heating process. Figure 1 illustrates synthetic procedure of s-$Ru_1Pt@W_1/NC$. First, as-fabricated porous NC was ground with $W(CO)_6$ to obtain $W(CO)_6/NC$. Next, $W(CO)_6/NC$ was pyrolyzed at 550 °C for 30 s in argon (Ar) atmosphere to obtain W_1/NC. Then, W_1/NC adsorbed Pt^{2+} and Ru^{3+} in deionized water was obtained and served as $Pt^{2+}/Ru^{3+}@W_1/NC$. Finally, s-$Ru_1Pt@W_1/NC$ was obtained by heating the $Pt^{2+}/Ru^{3+}@W_1/NC$ at 700 °C for 25 s (Supplementary Fig. 1). The s-$Pt@W_1/NC$, s-$Ru_1Pt@NC$, s-Pt/NC were prepared as control samples by the similar method. Transmission electron microscopy (TEM) was used for investigating the morphology of s-$Ru_1Pt@W_1/NC$ and control samples (Supplementary Fig. 2). Aberration-corrected high-angle annular dark-field scanning transmission electron microscopy (AC HAADF-STEM) was used to collect further micro-morphology information. From Fig. 2a, several tiny nanoparticles can be observed clearly on the porous NC. The PtRu nanoparticles whose average size are 2–3 nm with apparent lattice stripes (Supplementary Fig. 3). Dark areas that marked with orange circles in the lattice stripes can be identified as Ru atoms, which also confirms the formation of PtRu alloy (Fig. 2b). Meanwhile, plenty of single atoms that marked with red circles can be found, located around the PtRu alloy nanoparticles that marked with yellow circles in Fig. 2c. To maximize the accuracy of lattice spacing measurements, the lattice spacing of s-$Ru_1Pt@W_1/NC$ was obtained by calculating the average of several lattice distance 2.23 Å (111), which is smaller than the 2.27 Å of Pt(111), indicating lattice contraction from alloying Pt atoms (1.37 Å) with small-radius Ru atoms (1.33 Å), and pointing to the fact that W atoms (1.39 Å) with slightly larger atomic radius are not alloyed with Pt atoms. Moreover, isolated W and Ru atoms are distributed near tiny PtRu nanoparticles on porous NC. To further confirm the specific elements of single atoms, we selected an area containing only a few single atoms for electron energy loss spectroscopy (EELS) signal acquisition (Supplementary Fig. 4). The signal intensity peaks of Ru and W are at 2850 eV and 1800 eV respectively, corresponding to $L_{2,\ 3}$ and $M_{4,\ 5}$. Proving the existence of Ru and W single atoms on carbon support. Powder X-ray diffraction (XRD) analysis was employed to explore crystalline phase of s-$Ru_1Pt@W_1/NC$ (Supplementary Fig. 5). No apparent peak can be detected in the XRD pattern, due to the alloy particles are too small to be detected. The Brunauer-Emmett-Teller (BET) test for s-$Ru_1Pt@W_1/NC$ shows that it has a large specific surface area of 1145.34 m^2 g^{-1} (Supplementary Fig. 6). The energy dispersive X-ray (EDX) elemental mapping in Fig. 2d confirms that the distribution trajectories PtRu nanoparticles of Pt and Ru atoms are almost identical, whereas the distribution of W is more evenly distributed over the porous NC. This phenomenon is further evidence for the formation of Ru_1Pt single-atom alloy, without the formation of alloy from Pt and W atoms.

X-ray photoelectron spectroscopy (XPS) was utilized to characterize the chemical composition and valence states of the surface elements. In Fig. 2e, the Pt 4f spectra for s-$Ru_1Pt@W_1/NC$ show four deconvolved peaks at around 71.8, 72.9, 75.2, and 76.2 eV, which can be assigned to Pt^0 4$f_{7/2}$, Pt^{2+} 4$f_{7/2}$, Pt^0 4$f_{5/2}$ and Pt^{2+} 4$f_{5/2}$, respectively[6]. The Pt^0 4$f_{7/2}$ peak for s-$Ru_1Pt@W_1/NC$ shifted positively by 0.5 eV and 0.3 eV compared with those of s-Ru_1Pt/NC and s-Pt/NC, respectively. As shown in Fig. 2f, the four deconvolved peaks in the Ru 3p spectrum of s-$Ru_1Pt@W_1/NC$ located at around 461.8, 464.9, 484.3, and 486.7 eV are assigned to Ru^0 3$p_{3/2}$, Ru^{x+} 3$p_{3/2}$, Ru^0 3$p_{1/2}$, and Ru^{x+} 3$p_{1/2}$, respectively[27]. The Ru^0 3$p_{3/2}$ peak for s-$Ru_1Pt@W_1/NC$ shifted positively by 0.4 eV compared to s-Ru_1Pt/NC. In Supplementary Fig. 7, there are the four deconvolved peaks in the W 4 f spectrum of s-$Ru_1Pt@W_1/NC$ can be observed at 33.3, 34.6, 35.8, and 37.2 eV are assigned to W^{4+} 4$f_{7/2}$, W^{4+} 4$f_{5/2}$, W^{6+} 4$f_{7/2}$, and W^{6+} 4$f_{7/2}$, respectively[28]. Compared with W_1/NC, the W peak for s-$Ru_1Pt@W_1/NC$ negatively shifts 0.1 eV, demonstrating the existence of the electron transfer from Pt to W. From Figs. 2e, f and Supplementary Fig. 7, there is an electron transfer between Pt and Ru and W due to the introduction of Ru and W atoms, implying that the long-range W atoms and the near-range Ru atoms synergistically regulate the electronic structure of Pt. Besides, Supplementary Fig. 8a shows N 1s spectrum, which is divided into four peaks, pyridine N (398.6 eV), graphite N (401.1 eV), oxidized N (402.7 eV) and metal N (399.9 eV)[3]. And O 1s spectrum in Supplementary Fig. 8b can be assigned to M-O (529.9 eV), C = O (531.7 eV), and O = C-O (533.8 eV)[29].

Atomic structure analysis

The atomic-level structure of s-$Ru_1Pt@W_1/NC$ was investigated using X-ray absorption spectroscopy (XAS). According to X-ray absorption near-edge structure (XANES) spectra at Pt L_3-edge of s-$Ru_1Pt@W_1/NC$, Pt foil, and PtO_2 (Fig. 3a), we observe that the valence state of Pt is located between Pt foil (0) and PtO_2 (+4), approaching the Pt foil. The extended X-ray absorption fine structure (EXAFS) was attained by

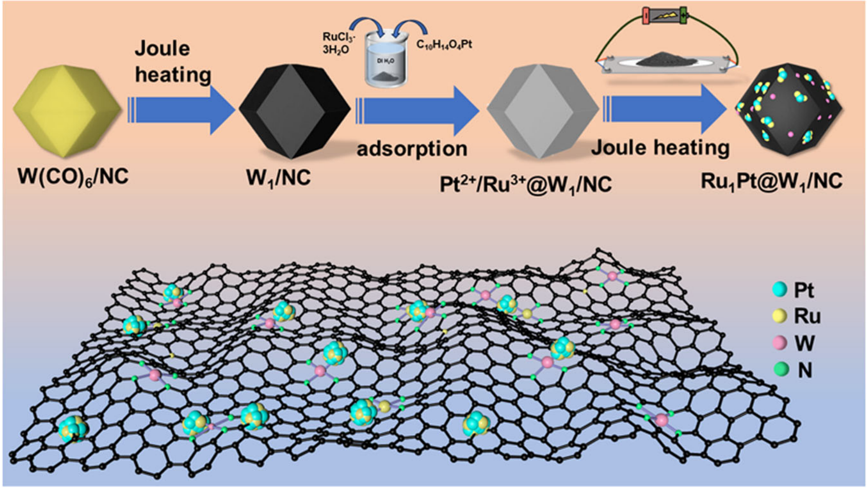

Fig. 1 | Synthesis of catalyst. Preparation of *s*-Ru$_1$Pt@W$_1$/NC.

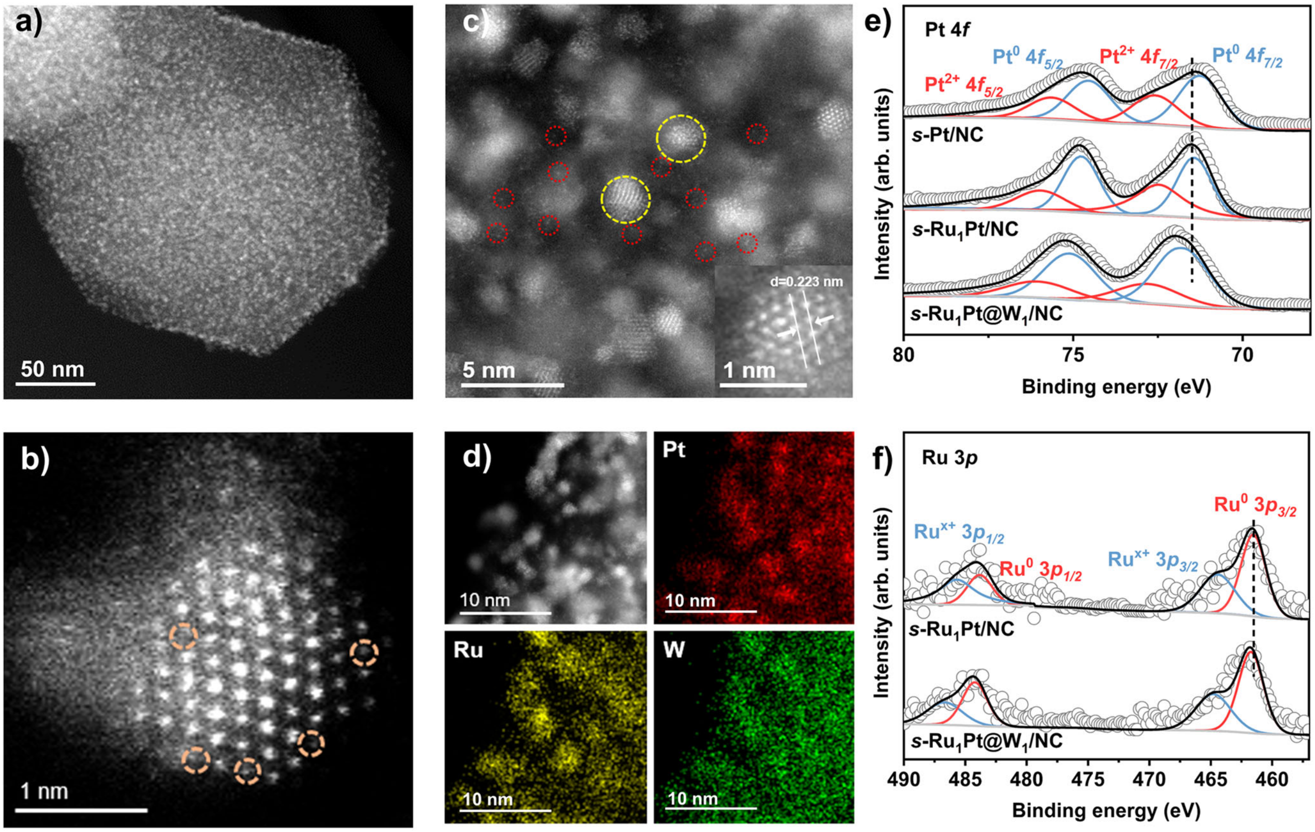

Fig. 2 | Characterizations of catalysts. a AC HAADF-STEM image of *s*-Ru$_1$Pt@W$_1$/NC. **b** AC HAADF-STEM image of *s*-Ru$_1$Pt@W$_1$/NC (the spots in the orange dashed circles are ascribed to Ru atoms). **c** AC HAADF-STEM image of *s*-Ru$_1$Pt@W$_1$/NC (the spots in the yellow and red dashed circles are ascribed to the alloy nanoparticles and the single atoms, respectively), inset of c) is the AC HAADF-STEM image for measuring the lattice distance. **d** HAADF-STEM images of the Pt, Ru and W distribution. **e** Pt 4*f* XPS spectra of *s*-Pt/NC, *s*-Ru$_1$Pt/NC and *s*-Ru$_1$Pt@W$_1$/NC. **f** Ru 3*p* XPS spectra of *s*-Ru$_1$Pt/NC and *s*-Ru$_1$Pt@W$_1$/NC. Source data for XPS are provided as a Source Data file.

Fourier transform for revealing the local atomic coordination structures of Pt. The k^3-weighted Fourier transform curves at R space of Pt L$_3$-edge EXAFS spectra for *s*-Ru$_1$Pt@W$_1$/NC, Pt foil and PtO$_2$ are displays in Fig. 3b. The strong Fourier transform peak of Pt in *s*-Ru$_1$Pt@W$_1$/NC is located between 2-3 Å, with a peak shape like Pt foil, and is assigned to Pt-Pt/Ru scattering. Moreover, the strong peak is negatively shifted to 2.51 Å compared to 2.57 Å in the Pt foil (Fig. 3b). Depending on the fitting results, the main peak at 2.51 Å that assigns to Pt-Pt/Ru coordination at the first shell confirms the formation of PtRu alloy (Supplementary Figs. 9a, 10a). For further confirmation, wavelet transforms (WT) were applied to *s*-Ru$_1$Pt@W$_1$/NC, Pt foil and PtO$_2$. The maximums of the WT signal of Pt L$_3$-edge in *s*-Ru$_1$Pt@W$_1$/NC emerged at 10.60 Å^{-1}, which is imputable for the Pt-Pt/Ru paths (Fig. 3c). To further confirm the atomic-level structure of Ru and W, we conducted the same characterization and analysis. From the Ru K-edge XANES spectra, the absorption edge of Ru is located between Ru foil and RuO$_2$ (Fig. 3d), implying that the valence state of Ru is between 0 and +4. The corresponding Ru K-edge EXAFS spectra of *s*-Ru$_1$Pt@W$_1$/NC showed

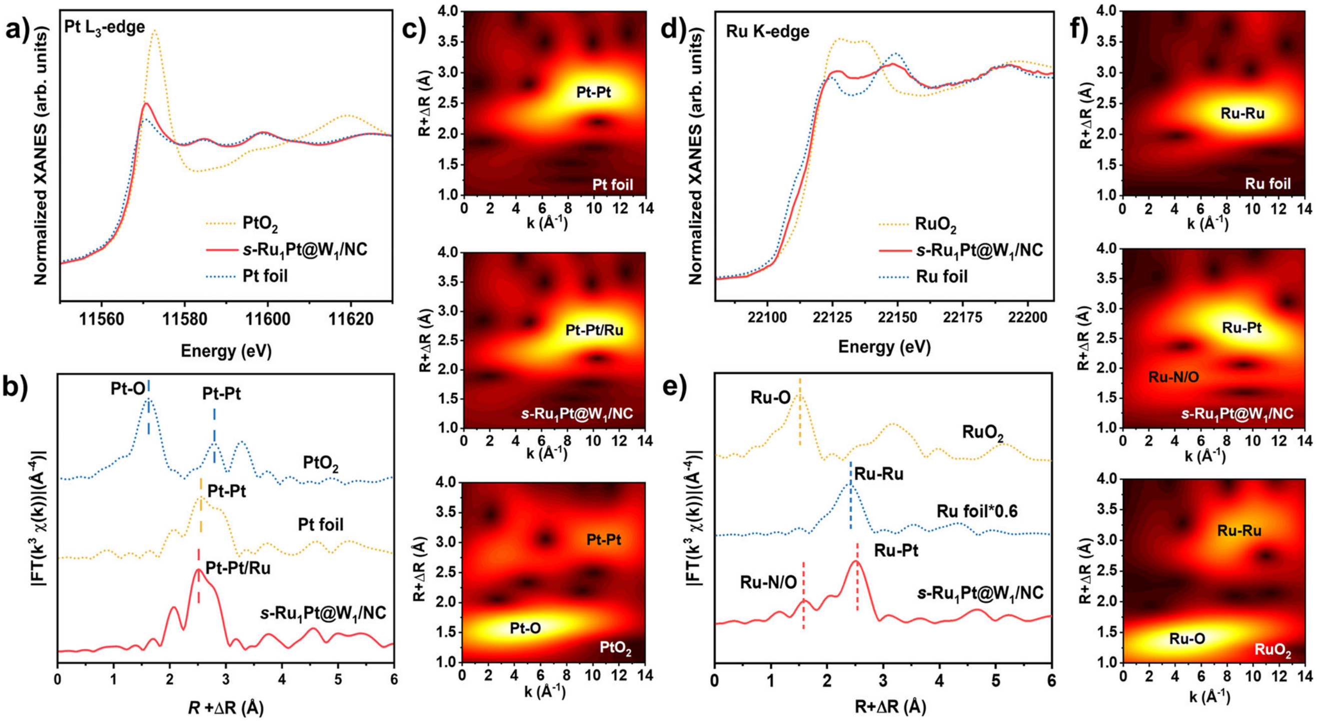

Fig. 3 | Electronic structure characterizations of catalysts. **a** The Pt L_3-edge XANES spectra of *s*-$Ru_1Pt@W_1/NC$, Pt foil and PtO_2. **b** FT-EXAFS spectra at the Pt L_3-edge of Pt foil, PtO_2 and *s*-$Ru_1Pt@W_1/NC$. **c** Pt L_3-edge WT-EXAFS of Pt foil, PtO_2 and *s*-$Ru_1Pt@W_1/NC$. **d** Normalized XANES spectra at the Ru K-edge of *s*-$Ru_1Pt@W_1/NC$, Ru foil and RuO_2. **e** FT-EXAFS spectra at the Ru K-edge of *s*-$Ru_1Pt@W_1/NC$, Ru foil and RuO_2. **f** Ru K-edge WT-EXAFS of *s*-$Ru_1Pt@W_1/NC$, Ru foil and RuO_2. Source data for XAS are provided as a Source Data file.

two peaks, one of the peaks is located at 2.57 Å, with a positive shift compared to Ru foil (2.40 Å), indicating that the alloying of Ru with larger radius Pt atoms (Fig. 3e). This is consistent with the results observed in the Pt L_3-edge EXAFS spectra. In addition, the peak of Ru-N/O located at 1.60 Å can also be observed, confirming the existence of some Ru in single-atom form. Moreover, did not find the high shell peak at 3.15 Å belonging to Ru-O-Ru, implying the absence of Ru in the form of RuO_x. Overall, these indicates that Ru in *s*-$Ru_1Pt@W_1/NC$ exists in the form of single atoms on the N-doped carbon support and single atom alloys. Based on the results of the fitting, the longer bond at 2.57 Å is attributed to the Pt-Ru scattering path rather than to Ru-Ru and the peak at 1.60 Å assigns to Ru-N/O (Supplementary Figs. 9b, 10b). The WT signal of the Ru K-edge in *s*-$Ru_1Pt@W_1/NC$ shows the coordination features, verifying that Ru exists in the form of Ru-Pt and Ru-N/O. Similarly, the XANES spectra of W L_3-edge in Supplementary Fig. 11a, the white line peak of *s*-$Ru_1Pt@W_1/NC$ located in the middle of W foil and WO_3, indicating W existing in the oxidation state and the valence state of W stays between 0 and +6 (Supplementary Fig. 11a). The W-L_3 edge FT-EXAFS spectrum of *s*-$Ru_1Pt@W_1/NC$ has a peak centered at 1.20 Å like that of WO_3, assigned to the W-N/O scattering path (Supplementary Fig. 11b). In addition, no peak at 2.60 Å similar to W foil and no obvious peak at the high shell position were detected on the curve, providing strong evidence that W exists in atomic dispersion and the absence of W in the form of WO_x, which is consistent with lattice distance and EDX elemental mapping. The fitting results in Supplementary Figs. 9c, 10c and Supplementary Table 1 demonstrate the W single atoms that coordinate with N/O from nitrogen-doped carbon and the long-range non-bonded electronic mutual interactions between W and Pt/Ru maybe present[30]. The intensity maximum of the WT signal of the W L_3-edge in *s*-$Ru_1Pt@W_1/NC$ occurs at 7.70 $Å^{-1}$, which can be attributed to the W-N/O (Supplementary Fig. 11c). Thus, we infer that Pt and Ru exist in the form of Ru_1Pt single-atom alloy nanoparticles and W in the form of single atoms coordinated with N/O is located around the Ru_1Pt on porous NC.

Evaluation of HOR performance

The electrocatalytic HOR performance of *s*-$Ru_1Pt@W_1/NC$, commercial PtRu/C and Pt/C were explored on a rotating disk electrode (RDE) in 0.10 M H_2-saturated KOH solution with a standard three-electrode system at a scan rate of 10 mV s^{-1} (Supplementary Figs. 12, 13). At the same time, *s*-Ru_1Pt/NC, *s*-$Pt@W_1/NC$ and *s*-Pt/NC were tested for studying the active source. According to Fig. 4a and Supplementary Fig. 14, with potential increased, the anode current of *s*-$Ru_1Pt@W_1/NC$ increased apace, having the highest limit current, exhibiting better HOR activity than those of commercial PtRu/C as well as Pt/C and other controls for HOR in alkaline electrolyte. And non-iR corrected profiles are provided in Supplementary Figs. 13 and 14a. We then tested the polarization curve of the *s*-$Ru_1Pt@W_1/NC$ in Ar-saturated 0.10 M KOH and found that the anode current was negligible, indicating that the current density originated from HOR (Supplementary Fig. 15). Moreover, it can be observed that the current densities of commercial PtRu/C and *s*-Ru_1Pt/NC drop sharply around 0.10 V vs. RHE (Fig. 4a). This is because the excessive oxidation of metal Ru species leads to the decrease of current, which leads to the disappearance of Ru sites bound to hydrogen[31,32]. In comparison, *s*-$Ru_1Pt@W_1/NC$ performed tiny falling at 0.10 V vs. RHE. It was shown that the doping of W inhibited the oxidation of Ru, which play a significant role in improving the overall stability of the catalysts.

The better HOR activity of *s*-$Ru_1Pt@W_1/NC$ than the other control catalysts were proved by the kinetic current density (j^k) extracted from Koutecky-Levich equation (Fig. 4b and Supplementary Fig. 16). And *s*-$Ru_1Pt@W_1/NC$ has the best kinetic activity. Polarization curves for *s*-$Ru_1Pt@W_1/NC$ and *s*-Ru_1Pt/NC at different rotation speeds were gleaned in Supplementary Fig. 17. As the rotational speed increases, the current intensity increases greatly due to the better mass transportation. The Koutechy-Levich plot slope of *s*-$Ru_1Pt@W_1/NC$ and *s*-Ru_1Pt/NC is 13.25 and 14.45 $cm^2 mA^{-1} rpm^{1/2}$ respectively, which is consistent with the two-electron HOR process[33]. To evaluate the intrinsic HOR activity of the studied catalysts, we calculated the exchange current density (j^0)

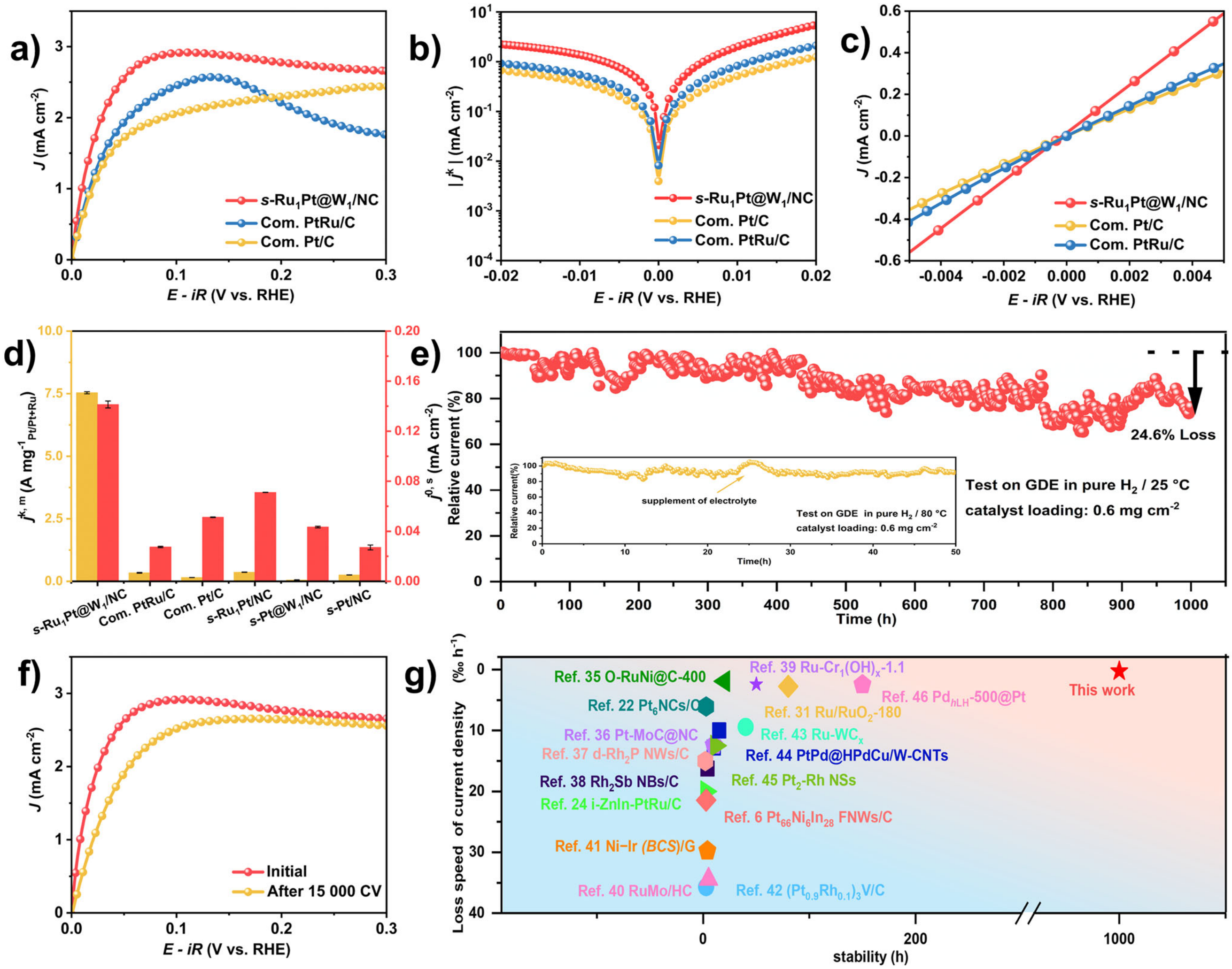

Fig. 4 | Electrocatalytic HOR performance. **a** HOR polarization curves of *s*-Ru$_1$Pt@W$_1$/NC, commercial PtRu/C and Pt/C in H_2 saturated 0.10 M KOH electrolyte with a scan rate of 10 mV s^{-1} and a rotation speed of 1600 rpm. The potentials are 95% *iR*-corrected and the R values for commercial PtRu/C, Pt/C, *s*-Ru$_1$Pt@W$_1$/NC measurements were 38.03, 37.83, 37.90 Ω, respectively. **b** Tafel plots derived from HOR polarization curves normalized kinetic current densities j^k via the Koutecky-Levich equation. The potentials are 95% *iR*-corrected (**c**) Linear fitting curves of *s*-Ru$_1$Pt@W$_1$/NC and the references in the micro-polarization region. The potentials are 95% *iR*-corrected. **d** Specific activity $j^{0,s}$ and the kinetic mass activity $j^{k,m}$ at 0.05 V vs. RHE of *s*-Ru$_1$Pt@W$_1$/NC and the references. Error bars show as mean s.d. **e** Chronoamperometry response of *s*-Ru$_1$Pt@W$_1$/NC in an H_2-saturated 0.10 M KOH at 0.05 V vs. RHE (inset: j-t response of *s*-Ru$_1$Pt@W$_1$/NC in an H_2-saturated 0.10 M KOH at 0.05 V vs. RHE at 80 °C). **f** HOR polarization curves of *s*-Ru$_1$Pt@W$_1$/NC before and after 15 000 CV cycles of ADT in H_2-saturated 0.10 M KOH. The potentials are 95% *iR*-corrected (**g**) Comparison of stability and loss speed of current density for HOR reported lately. Source data for electrochemical testing are provided as a Source Data file.

by fitting the linear region of micro-polarization and the fitting of the Butler-Volmer equation (Figs. 4c, Supplementary Fig. 18, 19 and Table 2). The electrochemical surface area (ECSA) was measured using the copper underpotential deposition (Cu-UPD) (Supplementary Fig. 20). We used ECSA to normalize j^0 and obtained specific activity $j^{0,s}$, as shown in Fig. 4d and Supplementary Table 2. The specific activity of *s*-Ru$_1$Pt@W$_1$/NC was found to be 5 times and 2 times higher than those of commercial PtRu/C and Pt/C, respectively. Additionally, the noble metal content in *s*-Ru$_1$Pt@W$_1$/NC was measured using inductively coupled plasma optical emission spectroscopy (ICP-OES), revealing Pt, Ru, and W contents of 3.81 %, 0.37 %, and 0.43 %, respectively (Supplementary Table 3). Furthermore, we normalized j^k by the noble metal content to obtain the kinetic mass activity. The kinetic mass activity of *s*-Ru$_1$Pt@W$_1$/NC was calculated to be 7.54 A mg$_{Pt+Ru}^{-1}$, significantly outperforming commercial PtRu/C (0.29 A mg$_{Pt+Ru}^{-1}$), commercial Pt/C (0.15 A mg$_{Pt}^{-1}$), and *s*-Ru$_1$Pt/NC (0.37 A mg$_{Pt+Ru}^{-1}$). The $j^{k,m}$, and $j^{0,s}$ values for each catalyst are summarized in Fig. 4d and Supplementary Table 2. To confirm data reproducibility, we conducted measurements for three data sets and plotted error bars accordingly. And Error bars show as mean standard deviation (s.d.). The above results demonstrate the reproducibility of the HOR performance of *s*-Ru$_1$Pt@W$_1$/NC.

Considering that Pt is the source of activity and Ru is used as a guest metal to modulate the activity of Pt, we investigated the effect of different Ru contents on the catalyst performance, recorded as *s*-Ru$_x$Pt@W$_1$/NC (x = 0, 1, 2 and 4). We tested the HOR polarization curves of these catalysts, obtained the Tafel plots from polarization curves based on the Koutecky-Levich equation, and provided the linear fitting curves in micro-polarization region (Supplementary Fig. 21). It is not difficult to see that *s*-Ru$_1$Pt@W$_1$/NC performs best. For a more precise comparison, we further normalized j^k and j^0 through measuring the metal content of different catalysts by ICP-OES and ECSA by Cu-UPD to more intuitively demonstrate the best HOR performance (Supplementary Table 2 and 3). *s*-Ru$_1$Pt@W$_1$/NC has the great activity (0.14 mA cm^{-2}) and the best mass activity (7.54 A mg$_{Pt+Ru}^{-1}$). Supplementary Fig. 22 shows the HAADF-STEM images of catalysts with different Ru contents. We can see that excessive Ru content can lead to

PtRu particle aggregation, affecting the uniform distribution of nanoparticles on the NC. In conclusion, we deduced that the electronic structure of Pt could not be further modulated at a Ru content of 0, which led to undesirable alkaline HOR activity. However, too high Ru content causes aggregation of active nanoparticles, which results in a decrease in the number of active sites and a reduction in catalyst performance. In order to verify who is the main source of HOR activity in the catalyst with single Ru atoms and Ru_1Pt alloy particles, we used the EDTA and KSCN poisoning methods reported in the literature[34]. As shown in Supplementary Fig. 23, when 1 mM EDTA was added to the electrolyte, we found that the polarization curve showed a slight decrease, while when 1 mM KSCN was added to the electrolyte, a sharp decrease was observed. Based on the different poisoning effects observed, we conclude that the HOR activity is mainly due to the Ru_1Pt nanoparticles, whereas the Ru single atoms anchored to the N-doped carbon contribute only partially.

Stability is one of the key factors that influence the practical application. Firstly, we used the chronoamperometric method to detect the stability of *s*-$Ru_1Pt@W_1$/NC on RDE, the current density with 6.2% loss after 20 hours at 0.05 V vs. RHE, demonstrating its great stability (Supplementary Fig. 24). To simulate the fuel cell environment, we used GDE to test the stability of the catalyst. On the GDE, the catalyst was affected by more severe environments, including inadequate hydrogen provision and inefficient substrate transportation[14]. Most impressively, *s*-$Ru_1Pt@W_1$/NC showed a current density with just 24.60 % decay after 1000 h at 0.05 V vs. RHE (Fig. 4e), which is the most stable catalyst we have ever known. Given this, we further tested the stability on GDE using the same method at 80 °C to further simulate the working environment of fuel cells. There's almost no attenuation after running for 50 h at 0.05 V vs. RHE (inset in Fig. 4e). To compare the stability of the *s*-$Ru_1Pt@W_1$/NC and control catalysts, we compared stability over a 24 h period. During this period, the current density of *s*-Ru_1Pt/NC, commercial Pt/C and PtRu/C have decreased by 15.33%, 71.42% and 52.39% respectively (Supplementary Fig. 25). Compared to others, *s*-$Ru_1Pt@W_1$/NC had no loss after 24 h testing. In addition, accelerated degradation test (ADT) was adopted to inspect the durability of *s*-$Ru_1Pt@W_1$/NC, and after 15 000 cycles of CV between 0 and 1.0 V vs. RHE, the HOR polarization curve displayed a decrease 13.40 % at 0.10 V vs. RHE, which is less than the commercial Pt/C and PtRu/C (Fig. 4f, Supplementary Fig. 26 and Table 4). We also made a comparison of the changes in current density before and after ADT testing at 0.05 V vs. RHE and 0.20 V vs. RHE. And the less current density loss of *s*-$Ru_1Pt@W_1$/NC proved its great stability (Supplementary Table 4). We also tested the XPS and high-resolution transmission electron microscopy (HRTEM) of the *s*-$Ru_1Pt@W_1$/NC after 15 000 CV cycles ADT. There was no significant change in the chemical valence state of Pt, Ru, and W. Moreover, there was no significant change in the lattice spacing of the nanoparticles measured by HRTEM, indicating its superior stability (Supplementary Figs. 27 and 28). Moreover, *s*-$Ru_1Pt@W_1$/NC exhibits impressive long-term stability, mass activity and slow loss speed of current density compared to recently reported noble-metal based catalysts (Figs. 4g, Supplementary Fig. 29 and Table 5)[6,22,24,35–46].

Apart from high electrocatalytic activity and impressive durability, anti-CO poisoning capability is another indispensable feature for great HOR electrocatalysts. This is because the Pt surface preferentially binds to CO, causing denaturation of the active sites for *H adsorption/desorption[23]. The polarization curve of the *s*-$Ru_1Pt@W_1$/NC diminished 13.6% at 0.1 V (vs. RHE) in 1000 ppm CO/H_2 0.10 M KOH solution while the commercial PtRu/C decreased 14.3% and commercial Pt/C 47.5%. (Figs. 5a, Supplementary Fig. 30). We also used the chronoamperometry to test the resistance to CO toxicity of the *s*-$Ru_1Pt@W_1$/NC (Fig. 5b). After running for 5000 s, the current of *s*-$Ru_1Pt@W_1$/NC remained at 82.80 %, while commercial Pt/C and PtRu/C completely lost their activity at 1850 s and 2780 s, respectively. For searching the reason of the difference among the CO-tolerance property and activity of different catalysts, we conducted CO stripping experimentation[47]. As shown in Fig. 5c, owing to the oxidation of adsorbed CO, a strong oxidation peak appeared above 0.81 V vs. RHE was observed in the CO stripping curve of *s*-Pt/NC. After the addition of oxygenophilic Ru, the position of the CO oxidation peak shifted negatively, indicating an enhanced adsorption of *OH. The addition of W further produced this result, as the CO oxidation peak of *s*-Ru_1Pt/NC shifted negatively 0.68 V vs. RHE, which is more negative than *s*-Pt/NC 0.81 V vs. RHE and *s*-Ru_1Pt/NC 0.78 V vs. RHE. Therefore, *s*-$Ru_1Pt@W_1$/NC has the strongest affinity with *OH, which is solid evidence to explain the enhanced activity for HOR in alkaline media[32].

Inspired by the surprising alkaline HOR performance of *s*-$Ru_1Pt@W_1$/NC, we investigated the HER property of *s*-$Ru_1Pt@W_1$/NC. The *s*-$Ru_1Pt@W_1$/NC and commercial Pt/C were evaluated on the RDE in 1.0 M KOH solution. As shown in Supplementary Fig. 31, *s*-$Ru_1Pt@W_1$/NC has a prominent property, with an overpotential of 15 mV at a current density of 10 mA cm^{-2}, which is more advanced than that of commercial Pt/C (34 mV). As shown in Supplementary Fig. 31b, the Tafel slope of *s*-$Ru_1Pt@W_1$/NC (33 mV dec^{-1}) is lower than commercial Pt/C (106 mV dec^{-1}), indicating that it has a better kinetic activity[48]. In addition, *s*-$Ru_1Pt@W_1$/NC also demonstrated superior stability tested by ADT and chronoamperometry, respectively. After 10 000 CV cycles of ADT, the overpotential at a current density of 10 mA cm^{-2} increased slightly, and after running for 10 000 s at this current density, the potential remained almost unchanged (Supplementary Fig. 32).

More insights from DFT calculations

We further investigated the reasons for the great HOR activity, long-term stability, and CO resistance of *s*-$Ru_1Pt@W_1$/NC through DFT calculations. Based on existing experimental data, we have reasonably designed relevant computational models. We constructed a model of PtRu single atom alloy with Ru introduced into the Pt subsurface coexisting with Ru and W single atoms on a carbon support, and also constructed a series of controls for comparison, namely *s*-$Ru_1Pt@W_1$/NC, Pt(111), PtRu, *s*-Pt/NC, *s*-Ru_1Pt/NC and *s*-$Pt@W_1$/NC (Supplementary Figs. 33–35). *H and *OH are two important intermediates in the alkaline HOR process. To ensure the rigor of intermediate adsorption energy testing, we selected multiple different sites for intermediate adsorption strength testing, and ultimately selected the optimal adsorption site to calculate the adsorption energy of each model (Supplementary Figs. 36–38). Therefore, to gain a deeper understanding of the sources of performance of *s*-$Ru_1Pt@W_1$/NC, we tested the adsorption of intermediates in different models. As shown in Fig. 5d, compared to Pt(111) (-0.31 eV), PtRu (-0.38 eV), *s*-Ru_1Pt/NC (-0.41 eV), *s*-$Pt@W_1$/NC (-0.43 eV) and *s*-Pt/NC (-0.48 eV), *s*-$Ru_1Pt@W_1$/NC stands out with the optimal ΔG_{*H} of -0.28 eV. The ΔG_{*H} closer to 0 eV indicates a weakened binding of *H adsorbed on the catalyst surface, ensuring its rapid conversion and accelerating the progress of HOR. Meanwhile, the adsorption energy of *OH (ΔG_{*OH}) was calculated (Fig. 5e). The *OH adsorption affects the reaction speed of the Volmer reaction as the rate-determining step (RDS)[33]. Therefore, great alkaline HOR catalysts should provide adsorption that satisfies the rapid occurrence of the Volmer step. With the introduction of Ru atoms, the ΔG_{*OH} of Pt(111) and *s*-$Pt@W_1$/NC decreased from 0.81 eV and -0.18 eV to -0.20 eV (PtRu) and -0.25 eV (*s*-$Ru_1Pt@W_1$/NC), respectively. The introduction of Ru atoms increases the *OH adsorption and improves the rapid binding rate between *OH and *H to the extent of improving the HOR performance. This is consistent with the experimental results of CO-stripping (Fig. 5c). To explain this change, we calculated the projected density of states (PDOS) and *d*-band center for each of the four catalysts s-Pt/NC and s-$Pt@W_1$/NC (with Ru and without Ru) (Fig. 5f). The results proved that *s*-Pt/NC vs. *s*-Ru_1Pt/NC, *s*-$Pt@W_1$/NC vs. *s*-$Ru_1Pt@W_1$/NC, *d*-band center upshift from -2.17 eV and -2.18 eV to

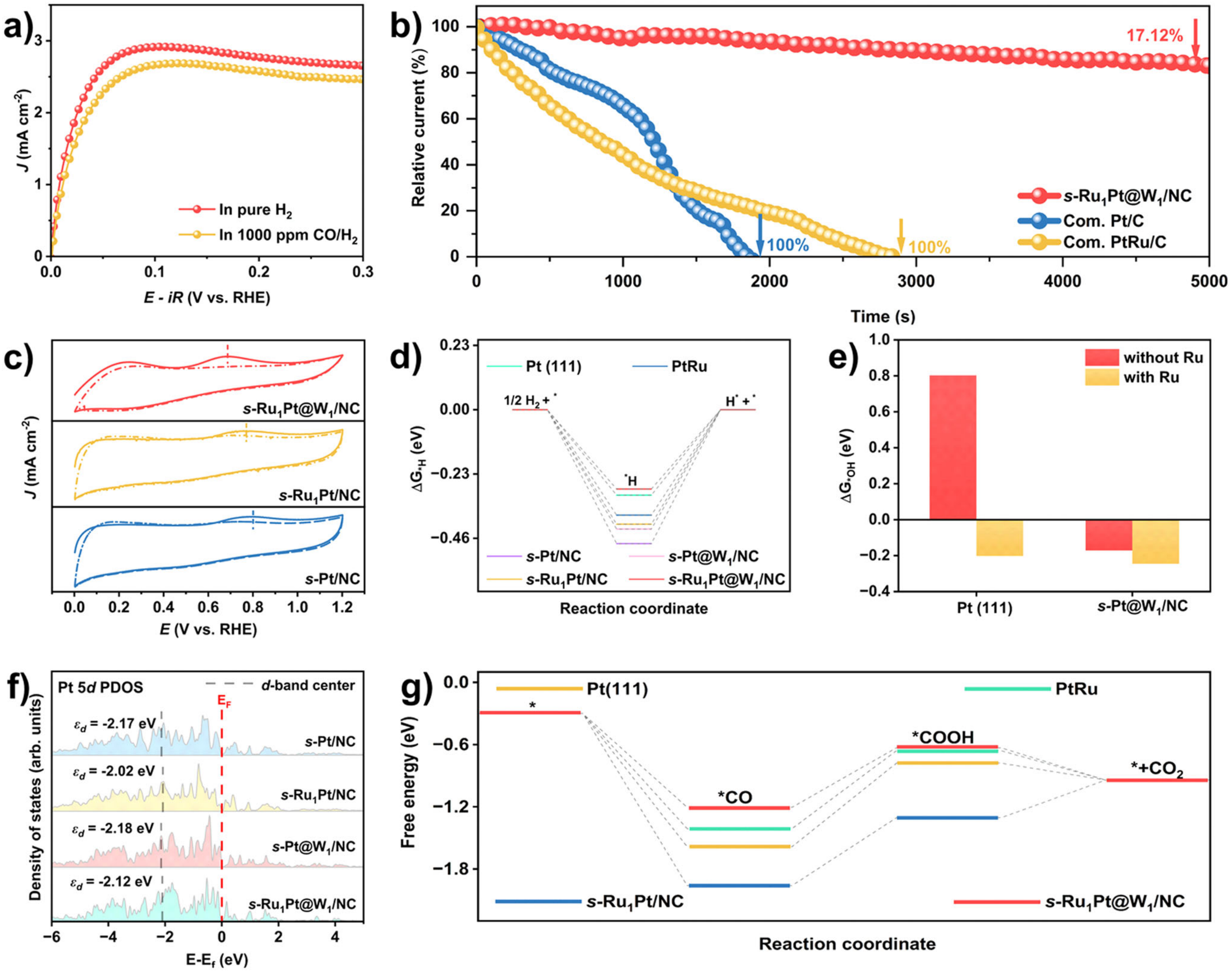

Fig. 5 | **Theoretical investigation. a** HOR polarization curves of *s*-$Ru_1Pt@W_1/NC$ in 1000 ppm CO/H_2-saturated 0.10 M KOH. The potentials are 95% *iR*-corrected and the R values for *s*-$Ru_1Pt@W_1/NC$ measurement was 37.90 Ω. **b** Comparison of the stability of *s*-$Ru_1Pt@W_1/NC$ and the references in 1000 ppm CO/H_2-saturated 0.10 M KOH solution tested on RDE. **c** CO-stripping of *s*-$Ru_1Pt@W_1/NC$ and the references (The solid line is the first lap and the dotted line is the second lap). **d** Free energy of *H adsorption on Pt(111), PtRu, *s*-Pt/NC, *s*-$Pt@W_1/NC$, *s*-Ru_1Pt/NC and *s*-$Ru_1Pt@W_1/NC$. **e** Comparison of *OH adsorption energy of Pt(111), PtRu, *s*-$Pt@W_1/NC$ and *s*-$Ru_1Pt@W_1/NC$. **f** The PDOS of *s*-Pt/NC, *s*-Ru_1Pt/NC, *s*-$Pt@W_1/NC$ and *s*-$Ru_1Pt@W_1/NC$. **g** Free energy of CO adsorption and oxidation process on Pt(111), PtRu, *s*-Pt/NC, *s*-$Pt@W_1/NC$, *s*-Ru_1Pt/NC and *s*-$Ru_1Pt@W_1/NC$. Source data for electrochemical testing and DFT calculations are provided as a Source Data file.

-2.02 eV and -2.12 eV, respectively. It is illustrated that the *OH adsorption is enhanced by introducing long-range W atoms and near-range Ru atoms, benefiting the combination of *OH and *H. Moreover, it can be seen from Supplementary Fig. 39 that *s*-$Ru_1Pt@W_1/NC$ has the weakest adsorption of H_2O, ensuring the rapid desorption of H_2O and the unoccupied active site[49]. In addition, we also demonstrated the source of the stability of *s*-$Ru_1Pt@W_1/NC$ by calculating the formation energy and dissolution energy of the catalyst (Supplementary Figs. 40 and 41). The low formation energy and high dissolution energy indicate that the introduction of W and Ru greatly improves the thermodynamic stability of the *s*-$Ru_1Pt@W_1/NC$. To verify the CO tolerance of the *s*-$Ru_1Pt@W_1/NC$, the free energy of *CO adsorption and oxidation was calculated (Fig. 5g) (The adsorption model is shown in the Supplementary Fig. 42). The *CO adsorption energy of *s*-$Ru_1Pt@W_1/NC$, Pt(111) and PtRu is -0.90 eV, -1.28 eV and -1.11 eV, respectively. It shows that the *CO adsorption has reduced, reducing the poisoning effect. Additionally, the oxidation of *CO to *COOH is considered the RDS, which determines the rate of CO conversion[14]. In *s*-$Ru_1Pt@W_1/NC$, the energy change between *CO and *COOH (-0.60 eV) is lower than those of Pt(111) (-0.80 eV) and *s*-Ru_1Pt/NC (-0.76 eV), indicating that CO has a short residence time on the *s*-$Ru_1Pt@W_1/NC$ surface and contributes to the promotion of the CO oxidation. Therefore, it can be seen that the synergistic regulation of near-range atoms and long-range atoms has jointly optimized the *H, *OH and *CO adsorption on the surface of Pt nanoparticles, accelerated the *CO oxidation, and improved the dissolution energy of the *s*-$Ru_1Pt@W_1/NC$. Therefore, *s*-$Ru_1Pt@W_1/NC$ has impressive alkaline HOR performance, CO resistance, and long-term stability.

Discussion

In summary, we successfully anchored ultrafine Ru_1Pt single-atom alloy nanoparticles on porous NC modified by W single atoms via Joule heating. Most impressive is its outstanding stability, stable at 0.05 V vs. RHE in 0.10 M KOH for 1000 h. During long-term HOR operation, thanks to the interaction of Ru_1Pt single-atom alloy nanoparticles on single atoms W, the metals of *s*-$Ru_1Pt@W_1/NC$ were not oxidized, which might be the reason for its long-term stability. Its outstanding mass activity of 7.54 A mg_{Pt+Ru}^{-1} is much better than those of commercial PtRu/C and Pt/C. DFT calculations show modification of Ru_1Pt single-atom alloy nanoparticles with W loaded NC substrates significantly improves alkaline HOR performance. The introductions of oxyphilic species Ru and W optimize the binding energies of *H, *OH and *CO enables high activity and CO tolerance. The successful preparation of *s*-$Ru_1Pt@W_1/NC$ with low noble metal loading by Joule heating is one of the most advanced catalysts reported so far.

Methods

Materials

The chemicals and reagents were used as received. Analytical grade zinc nitrate hexahydrate ($Zn(NO_3)_2 \cdot 6H_2O$, 99%), Ruthenium trichloride trihydrate ($RuCl_3 \cdot 3H_2O$, 99%), 2-methylimidazole ($C_4H_6N_2$, 98%), Tungsten hexacarbonyl ($W(CO)_6$, 98%) and Acetylacetone platinum ($C_{10}H_{14}O_4Pt$, 98%, Pt 48%), Potassium hydroxide (KOH, 99%) were purchased from Adamas. Doubly distilled deionized water (18.2 MΩ) was used for all experiments.

Synthesis of ZIF-8. Generally, Zn $(NO_3)_2 \cdot 6H_2O$ (1.67 g, 5.614 mmol) and 2-methylimidazole (1.85 g, 22.531 mmol) were dissolved into 45 mL of methanol, respectively. Equal volumes of the above two solutions were mixed under stirring. After 20 h agitation for further reaction at room temperature, the as-obtained ZIF-8 product was collected by centrifugation (9000 rpm for 3 minutes) and washed with methanol 3 times and finally dried at 65 °C for 8 h in vacuum oven.

Synthesis of Porous NC. The above dried ZIF-8 is pyrolyzed at 900 °C for 2 h in a tube furnace under Ar atmosphere (heating rate 5 °C min^{-1}) to obtain the multi-void nitrogen-doped carbon.

Synthesis of *s*-$Ru_1Pt@W_1/NC$. Take 100 mg of pyrolyzed porous carbon and $W(CO)_6$ (7.04 mg, 0.020 mmol) into a mortar, grinding it for 30 minutes to obtain a homogeneous mixture and denoted as $W(CO)_6/NC$. And take 10 mg $W(CO)_6/NC$ on carbon paper and pyrolyzed at 90 A, 1.5 V under Ar atmosphere for 30 s for W_1/NC. Take 50 mg W_1/NC, with $C_{10}H_{14}O_4Pt$ (19.67 mg 0.050 mmol), $RuCl_3 \cdot 3H_2O$ (9.02 mg, 0.040 mmol) and add 30 ml of deionized water. After stiring at 80 °C for 3 h, centrifuge (12 000 rpm for 3 minutes) and dry in a vacuum oven at 65 °C for 8 h. After that, 10 mg of dried sample was taken on carbon paper and pyrolyzed at 100 A, 2 V under Ar atmosphere for 25 s to obtain *s*-$Ru_1Pt@W_1/NC$.

Synthesis of *s*-Ru_1Pt/NC, *s*-$Pt@W_1/NC$ and *s*-Pt/NC. *s*-Ru_1Pt/NC, *s*-$Pt@W_1/NC$ and *s*-Pt/NC were prepared in the same way as for *s*-$Ru_1Pt@W_1/NC$. The difference is that the corresponding metals were added in the preparation of the respective samples.

Material characterizations

The microstructure and morphology of the prepared materials was observed by transmission electron microscope (TEM; HT7800) and high-resolution transmission electron microscopy (HRTEM; FEI-Themis Z TEM/STEM operated at 300 kV and equipped with double spherical aberration (Cs) correctors, Themis Z TEM/STEM equipped with high angle annular dark field (HAADF) and annular bright field (ABF) detectors). High angle annular dark field (HAADF) images were acquired using the Themis Z with a 59 ~ 100 mrad inner-detector angle. The attainable resolution of the probe defined by the objective prefield is 60 picometers. X-ray photoelectron spectrometer (XPS) was operated by a ULVAC PHI Quantera microscope machine. Inductively coupled plasma optical emission spectroscopy (ICP-OES) was performed on Optima 7300 DV. The X-ray absorption find structure spectra (Pt L_3-edge, W L_3-edge and Ru K-edge) were collected at BL14W1 station in Shanghai Synchrotron Radiation Facility.

Electrochemical measurements

All catalysts were prepared by blending 3.0 mg of catalyst with 480 µL ethanol and Nafion (5 wt%, 20 µL), followed by ultrasonication for 3 h to form homogeneous catalysts inks, catalyst with the concentration of 6 mg mL^{-1} was obtained. 5 - 10 µL of the catalyst ink was deposited on the working electrode, of which the loading mass of catalysts were 0.152–0.306 mg cm^{-2}.

Electrochemical performance of the catalysts was carried out on a CHI760E electrochemical station (Shanghai Chenhua Instrument Corporation, China) in 0.10 M KOH and 1.0 M KOH.

To prepare 0.1 M KOH and 1.0 M KOH, 2.801 g and 28.055 g KOH was put in 500 mL deionized water respectively.Afte ultrasonicating for 20 minutes, transfer the solution into volumetric flasks and store them at room temperature (298 (± 0.1) K) away from light. In the three-electrode system, glassy carbon electrode (diameter: 5 mm; area:0.19625 cm^2) was served as the working electrode, Ag/AgCl electrode and Platinum wire as the reference electrode and counter electrode. Before electrochemical testing, platinum sheets as the working electrode and counter electrode, hydrogen-saturated KCl saturated solution as electrolyte, test the CV curve in the -0.7 to -1.1 V range and find the position where the current is 0 A. The electrode potential for the reversible hydrogen reaction was obtained by repeating the measurement three times and averaging the values. In this work, all operation was performed at the constant temperature at 298 (± 0.1) K and all the measured potentials were converted to the reversible hydrogen electrode (RHE) by the equations: E (vs. RHE) = E (vs. Ag/AgCl) + 0.0591 × pH + 0.196 with 95% iR-compensation. The polarization curve was performed at a scan rate of 10 mV s^{-1} under the RDE rotation rate of 1600 rpm in the potential range from about -1.0 to -0.4 V in alkalin for samples. Accelerated durability test (ADT) for *s*-$Ru_1Pt@W/CN$ was operated by 15 000 CV cycles between 0–1.0 V vs. RHE under H_2-saturated electrolyte. The CO anti-poisoning tests were carried out in electrolyte purged with saturated 1000 ppm CO/H_2. Chronoamperometric tests were carried out under constant potential of 0.05 V vs. RHE in H_2-saturated and 0.10 V in 1000 ppm CO/H_2-saturated electrolyte. CO stripping curves of catalysts were performed in a N_2-saturated solution. Before the electrical test, a high-purity CO gas is introduced into the electrolyte for 30 minutes to form a CO-saturated solution, and the CO is adsorbed on the catalyst at a potential of 0.10 V vs. RHE for 20 minutes. Subsequently, N_2 is introduced and bubbled in solution for 30 min to remove residual CO. The CO stripping curves between 0 V and 1.20 V vs. RHE were collected at a scan rate of 50 mV s^{-1} for two cycles. Moreover, it was carbon paper that was used to as the electrode substrate to prepare the catalyst-modified GDE. The 100 µL of catalyst ink was coated the onto the carbon paper with an active area of 1 × 1 cm^2 and dried it at 40 °C for 3 hours. And the catalyst loading on GDE was 0.6 mg cm^{-2}. Chronoamperometric tests were carried out under a constant potential of 0.05 V vs. RHE in H_2-saturated 0.1 M KOH. The EIS was conducted in the frequency range of 0.01–100 kHz.

Kinetic current density (j^k) could be deduced from the Koutecky-Levich equation:

$$\frac{1}{j} = \frac{1}{j^k} + \frac{1}{j^d} = \frac{1}{j^k} + \frac{1}{B\omega^{1/2}C_0} \tag{1}$$

where *j*, B, c_0, and ω are the measured current density, the Levich constant, the solubility of H_2 (7.33×10^{-4} mol L^{-1}), and the speed of the rotating, respectively.

Exchange current density (j^0) could be extracted from the Butler-Volmer equation:

$$j^k = j^0 \left[e^{\frac{\alpha F}{RT}} - e^{\frac{-(1-\alpha)F}{RT}\eta} \right] \tag{2}$$

j^0 could be also obtained from the approximate Butler-Volmer equation:

$$j = j^0 \frac{\eta F}{RT} \tag{3}$$

where α, η, R, T and F represent the transfer coefficient, the overpotential, the universal gas constant (8.314 J $mol^{-1}K^{-1}$), the temperature in Kelvin (298 K) and the Faraday constant, respectively.

The electrocatalytic properties toward HER were evaluated using a RDE (Pine, diameter of 5 mm) with CHI 760E Electrochemical Workstation. An Ag/AgCl (saturated KCl solution) and a graphite rod were used as the reference electrode and counter electrode, respectively. Linear sweep voltammetry (LSV) was performed at a scan rate of 50 mV s^{-1} in N_2-saturated 1.0 M KOH solution. The Stability testing was conducted at a scan rate of 100 mV s^{-1} for 10 000 CV cycles by the ranges from −0.393 to 0.093 V vs. RHE. The Continuous potentiometric V-t measurement under a constant current density of 10 mA cm^{-2} were used to assess the durability of the electrocatalysts, with the catalysts loaded on carbon cloth at a loading of 0.306 mg cm^{-2}.

The electrochemically active surface area (ECSA) of various samples was determined using the Cu-UPD technique. Prior to Cu deposition, the electrodes underwent multiple cycles between 0 and 1.0 V in pure 0.1 M H_2SO_4 to establish the baseline. Subsequently, Cu-UPD stripping voltammetry (0.25–0.95 V, 10 mV s^{-1}) was conducted in an Ar-saturated 0.1 M H_2SO_4 solution with 2 mM $CuSO_4$ following Cu deposition at 0.25 V for 100 s. The ECSA value can be computed using the following equation:

$$ECSA\left(\frac{cm^2}{g}\right) = \frac{Q_{Cu}}{M\,420\mu C\,V\,cm^{-2}} \tag{4}$$

where M is the mass loading of metals on the electrode and V represents the scanning speed.

DFT calculations

Using periodic slab model, spin-polarized density generalized function theory calculations have been carried out in the Vienna ab initio simulation package (VASP)[50]. The generalized gradient approximation of the Perdew-Burke-Ernzerhof general function (GGA-PBE) is used to describe the electron exchange and interaction mechanism[51]. The projected augmented wave (PAW) method is used to calculate the electron-ion interaction with a plane-wave basis set defined by a kinetic energy of 500 eV[52]. To treat the long-range dispersion interactions between surfaces and adsorbed substances, the DFT-D3 method developed by Grimme is used[53]. The Monkhorst-Pack scheme uses k-point sampling on a (5 × 5 × 1) grid[54]. When the electron self-consistent iteration and the force reach 10^{-5}eV and 0.02 eV $Å^{-1}$ respectively, the geometry optimization and energy calculations are completed. All data of electronic structure calculations in DFT is provided in Supplementary data 1.

The HOR process is divided into two fundamental steps:

(1) Tafel : $H_2 + 2^* = 2^*H$
(2) Heyrovsky : $H_2 + OH^- + ^* = ^*H + H_2O + e^-$
(3) Volmer : $^*H + OH^- = ^* + H_2O + e^-$

where *H presents the adsorbed H on a catalyst site and the energy of H^+/e^- is approximately equal to the energy of 1/2 H_2 using Computational Hydrogen Electrode model[55].

The Gibbs Free Energy Change

The formula:

$$\Delta G = \Delta E + \Delta E_{ZPE} - T\Delta S \tag{5}$$

defines the Gibbs free energy change for each adsorbed intermediate under standard conditions. ΔE is the energy change calculated by DFT, and ΔE_{ZPE} is the zero point energy. T is the system's temperature (298.15 K), and ΔS is the entropy difference between the gas phase and the adsorption state.

Surface energy

The 6-layer Pt(111) plate was constructed for the Pt surface, with two bottom layers fixed and two top layers free, was fixed and two upper layers were free. The surface energy ($E_{surface}$ (n)) which can be used for the investigation of the position of the Ru atom doped in the Pt(111) surface from the thermodynamic point of view, from a thermodynamic point.

$$E_{surface}(n) = \frac{1}{2A}\left(E_{slab} - nE_{bulk}\right) \tag{6}$$

Where E_{slab}, E_{bulk} and A represent the energy of Pt(111) slab and Pt cell, and surface area.

Formation energy

The thermodynamic stability of these possiple catalysis can be expressed by the formation energy (E_f) as follows:

$$E_f = \frac{E_{slab} - mE_{bulk,A} - nE_{bulk,B}}{m+n} \tag{7}$$

Where E_{slab} is the total energy of a slab, $E_{bulk,A}$ and $E_{bulk,B}$ are the energies of per cell for A and B atom, respectively, and m and n represent the number of A and B.

Dissolution energy

The optimized catalyst precipitates a Pt atom and dissolves into the bulk phase. The positions of the atoms are relaxed at all, thus optimizing a most stable energy.

$$E_d = E_{slab,x-1} + E_{bulk,Pt} - E_{slab} + neU^0_{Pt} \tag{8}$$

Where E_d is the dissolution energy for each catalyst system, $E_{bulk,x-1}$ is the energy of the slab after the dissolution of one atom, and $E_{bulk,Pt}$ is the energy of bulk Pt. E_{slab} is the optimized energy of the slab, n is the number of transferred electrons, and U^0_{Pt} is the standard dissolution potential[56].

Data availability

Source data are provided with this paper.

References

1. Hyun, J. et al. Powering the hydrogen future: current status and challenges of anion exchange membrane fuel cells. *Energy Environ. Sci.* **16**, 5633–5662 (2023).
2. Adabi, H. et al. High-performing commercial Fe–N–C cathode electrocatalyst for anion-exchange membrane fuel cells. *Nat. Energy* **6**, 834–843 (2021).
3. Zhao, M. et al. A pH-universal ORR catalyst with single-atom iron sites derived from a double-layer MOF for superior flexible quasi-solid-state rechargeable Zn–air batteries. *Energy Environ. Sci.* **14**, 6455–6463 (2021).
4. Feng, J. et al. Iron, nitrogen co-doped carbon spheres as low cost, scalable electrocatalysts for the oxygen reduction reaction. *Adv. Funct. Mater.* **31**, 2102974 (2021).
5. Song, F. et al. Interfacing nickel nitride and nickel boosts both electrocatalytic hydrogen evolution and oxidation reactions. *Nat. Commun.* **9**, 4531 (2018).
6. Wang, L. et al. PtNi/PtIn-skin fishbone-like nanowires boost alkaline hydrogen oxidation catalysis. *ACS Nano* **17**, 17779–17789 (2023).
7. Firouzjaie, H. et al. Catalytic advantages, challenges, and priorities in alkaline membrane fuel cells. *ACS Catal* **10**, 225–234 (2019).
8. Durst, J. et al. New insights into the electrochemical hydrogen oxidation and evolution reaction mechanism. *Energy Environ. Sci.* **7**, 2255–2260 (2014).
9. Sheng, W. et al. Hydrogen oxidation and evolution reaction kinetics on platinum: acid vs alkaline electrolytes. *J. Electrochem. Soc.* **157**, B1529 (2010).

10. Zheng, J. et al. Universal dependence of hydrogen oxidation and evolution reaction activity of platinum-group metals on pH and hydrogen binding energy. *Sci. Adv.* **2**, e1501602 (2016).
11. Yang, Z. et al. Tailoring interfacial chemistry of defective carbon-supported Ru catalyst toward efficient and CO-tolerant alkaline hydrogen oxidation reaction. *Adv. Energy Mater.* **13**, 2300881 (2023).
12. Duan, Y. et al. Bimetallic nickel-molybdenum/tungsten nanoalloys for high-efficiency hydrogen oxidation catalysis in alkaline electrolytes. *Nat. Commun.* **11**, 4789 (2020).
13. Yang, Y. et al. Suppressing electron back-donation for a highly CO-tolerant fuel cell anode catalyst via cobalt modulation. *Angew. Chem. Int. Ed.* **61**, e202208040 (2022).
14. Chen, G. et al. Near-atomic-scale superfine alloy clusters for ultrastable acidic hydrogen electrocatalysis. *J. Am. Chem. Soc.* **145**, 22069–22078 (2023).
15. Zhao, G. et al. Non-platinum group metal electrocatalysts toward efficient hydrogen oxidation reaction. *Adv. Funct. Mater.* **31**, 2010633 (2021).
16. Duan, Y. et al. Interfacial engineering of Ni/V_2O_3 heterostructure catalyst for boosting hydrogen oxidation reaction in alkaline electrolytes. *Angew. Chem. Int. Ed.* **62**, e202217275 (2023).
17. Ni, W. et al. An efficient nickel hydrogen oxidation catalyst for hydroxide exchange membrane fuel cells. *Nat. Mater.* **21**, 804–810 (2022).
18. Huang, C. et al. In situ construction of Ni/$Ni_{0.2}Mo_{0.8}N$ heterostructure to enhance the alkaline hydrogen oxidation reaction by balancing the binding of intermediates. *Adv. Funct. Mater.* **33**, 2300593 (2023).
19. Huang, Z. et al. A highly efficient pH-universal HOR catalyst with engineered electronic structures of single Pt sites by isolated co atoms. *Adv. Funct. Mater.* **33**, 2306333 (2023).
20. Chen, Z. et al. Stabilizing Pt single atoms through Pt-Se electron bridges on vacancy-enriched nickel selenide for efficient electrocatalytic hydrogen evolution. *Angew. Chem. Int. Ed.* **62**, e202308686 (2023).
21. Yang, F. et al. Sub-3 nm Pt@Ru toward outstanding hydrogen oxidation reaction performance in alkaline media. *J. Am. Chem. Soc.* **145**, 27500–27511 (2023).
22. Wang, X. et al. Atomic-precision Pt_6 nanoclusters for enhanced hydrogen electro-oxidation. *Nat. Commun.* **13**, 1596 (2022).
23. Wang, X. et al. Embedding oxophilic rare-earth single atom in platinum nanoclusters for efficient hydrogen electro-oxidation. *Nat. Commun.* **14**, 3767 (2023).
24. Huang, Z. et al. Implanting oxophilic metal in PtRu nanowires for hydrogen oxidation catalysis. *Nat. Commun.* **15**, 1097 (2024).
25. Dong, Y. et al. Pb-modified ultrathin RuCu nanoflowers for active, stable, and CO-resistant alkaline electrocatalytic hydrogen oxidation. *Angew. Chem. Int. Ed.* **62**, e202311722 (2023).
26. Wang, P. et al. V-O species-doped carbon frameworks loaded with Ru nanoparticles as highly efficient and CO-tolerant catalysts for alkaline hydrogen oxidation. *J. Am. Chem. Soc.* **145**, 27867–27876 (2023).
27. Wang, C. et al. Local oxidation induced amorphization of 1.5-nm-Thick Pt-Ru nanowires enables superactive and CO-tolerant hydrogen oxidation in alkaline media. *Adv. Funct. Mater.* **33**, 2304125 (2023).
28. Jing, C. et al. Revealing the origin of single-atom W activity in H_2O_2 electrocatalytic production: charge symmetry-breaking. *Carbon Energy*. **6**, e581, (2024).
29. Lin, Z. et al. Tuning the p-Orbital electron structure of s-Block metal Ca enables a high-performance electrocatalyst for oxygen reduction. *Adv. Mater.* **33**, e2107103 (2021).
30. Jiao, L. et al. Non-bonding interaction of neighboring Fe and Ni single-atom pairs on MOF-derived N-doped carbon for enhanced CO_2 electroreduction. *J. Am. Chem. Soc.* **143**, 19417–19424 (2021).
31. Zhang, X. B. et al. Fast and durable alkaline hydrogen oxidation reaction at the electron-deficient ruthenium-ruthenium oxide interface. *Adv. Mater.* **35**, e2208821 (2023).
32. Zhou, Y. et al. Lattice-confined Ru clusters with high CO tolerance and activity for the hydrogen oxidation reaction. *Nat. Catal.* **3**, 454–462 (2020).
33. Zhang, J. et al. Atomic-thick metastable phase RhMo nanosheets for hydrogen oxidation catalysis. *Nat. Commun.* **14**, 1761 (2023).
34. Lu, B. et al. Ruthenium atomically dispersed in carbon outperforms platinum toward hydrogen evolution in alkaline media. *Nat. Commun.* **10**, 631 (2019).
35. Zhang, X. et al. Regulating the surface electronic structure of RuNi alloys for boosting alkaline hydrogen oxidation electrocatalysis. *ACS Mater. Lett.* **4**, 2097–2105 (2022).
36. Zhou, F. et al. Electron-distribution control via Pt/NC and MoC/NC dual junction: boosted hydrogen electro-oxidation and theoretical study. *J. Energy Chem.* **88**, 513–520 (2024).
37. Huang, H. et al. Breaking Surface Atomic Monogeneity of Rh_2P Nanocatalysts by Defect-Derived Phosphorus Vacancies for Efficient Alkaline Hydrogen Oxidation. *Angew. Chem. Int. Ed.* **62**, e202315752 (2023).
38. Zhang, Y. et al. Atomically Isolated Rh Sites within Highly Branched Rh_2Sb Nanostructures Enhance Bifunctional Hydrogen Electrocatalysis. *Adv. Mater.* **33**, 2105049 (2021).
39. Zhang, B. et al. Atomically dispersed chromium coordinated with hydroxyl clusters enabling efficient hydrogen oxidation on ruthenium. *Nat. Commun.* **13**, 5894 (2022).
40. Ma, M. et al. Mo-modified electronic effect on sub-2 nm Ru catalyst for enhancing hydrogen oxidation catalysis. *J. Mater. Chem. A* **11**, 10807–10812 (2023).
41. Tang, T. et al. Unconventional bilateral compressive strained Ni-Ir interface synergistically accelerates alkaline hydrogen oxidation. *J. Am. Chem. Soc.* **145**, 13805–13815 (2023).
42. Hou, Y. et al. Synergistic modulation of multiple sites boosts anti-poisoning hydrogen electrooxidation reaction with ultrasmall $(Pt_{0.9}Rh_{0.1})_3V$ ternary intermetallic nanoparticles. *Angew. Chem. Int. Ed.* **63**, e202402496 (2024).
43. Wang, L. et al. Stabilizing low-valence single atoms by constructing metalloid tungsten carbide supports for efficient hydrogen oxidation and evolution. *Angew. Chem. Int. Ed.* **62**, e202311937 (2023).
44. Yan, R. et al. PtPd atomic layer shelled PdCu hollow nanoparticles on partially unzipped carbon nanotubes for breaking the activity-stability trade-off toward the hydrogen oxidation reaction in alkaline media. *Nano Lett* **24**, 4849–4857 (2024).
45. Cai, J. et al. Host–guest ensemble effect on dual-Pt atom-on-Rh nanosheets enables high-efficiency and anti-CO alkaline hydrogen oxidation. *ACS Catal* **13**, 6974–6982 (2023).
46. Zhao, T. et al. Improving alkaline hydrogen oxidation through dynamic lattice hydrogen migration in Pd@Pt core-shell electrocatalysts. *Angew. Chem. Int. Ed.* **63**, e202315148 (2024).
47. Luo, H. et al. Amorphous MoO_x with high oxophilicity interfaced with PtMo alloy nanoparticles boosts anti-CO hydrogen electrocatalysis. *Adv. Mater.* **35**, e2211854 (2023).
48. Wei, W. et al. Strain effects in Ru-Au bimetallic aerogels boost electrocatalytic hydrogen evolution. *Small* **20**, 2310603 (2024).
49. Mu, X. et al. Symmetry-broken Ru nanoparticles with parasitic Ru-Co dual-single atoms overcome the volmer step of alkaline hydrogen oxidation. *Angew. Chem. Int. Ed.* **63**, e202319618 (2024).
50. Kresse, G. et al. Efficient iterative schemes for ab initio total-energy calculations using a plane-wave basis set. *Phys. Rev. B* **54**, 11169–11186 (1996).
51. Perdew, J. P. et al. Generalized gradient approximation made simple. *Phys. Rev. Lett.* **77**, 3865–3868 (1996).
52. Blöchl, P. E. Projector augmented-wave method. *Phys. Rev. B* **50**, 17953–17979 (1994).

53. Grimme, S. et al. A consistent and accurate ab initio parametrization of density functional dispersion correction (DFT-D) for the 94 elements H-Pu. *J. Chem. Phys.* **132**, 154104 (2010).
54. Monkhorst, H. J. et al. Special points for Brillouin-zone integrations. *Phys. Rev. B* **13**, 5188–5192 (1976).
55. Nørskov, J. K. et al. Origin of the overpotential for oxygen reduction at a fuel-cell cathode. *J. Phys. Chem. B* **108**, 17886–17892 (2004).
56. Greeley, J. et al. Electrochemical dissolution of surface alloys in acids: thermodynamic trends from first-principles calculations. *Electrochim. Acta.* **52**, 5829–5836 (2007).

Acknowledgements

This work is supported by the National Natural Science Foundation of China (22102132), the Funds for Basic Scientific Research in Central Universities, the Marsden Fund Council from Government funding, managed by Royal Society Te Apārangi. Z.W. and R.L. wish to acknowledge the use of New Zealand eScience Infrastructure (NeSI) high performance computing facilities, consulting support and/or training services as part of this research. New Zealand's national facilities are provided by NeSI and funded jointly by NeSI's collaborator institutions and through the Ministry of Business, Innovation & Employment's Research Infrastructure program. URL https://www.nesi.org.nz. We thank the BL14W1 station in Shanghai Synchrotron Radiation Facility (SSRF) and 1W1B station for XAFS measurement in Beijing Synchrotron Radiation Facility (BSRF).

Author contributions

Y.H. conceived and supervised the research. W.J., Z.R., Z.C., and C.M. contributed equally to this work. W.J. carried out the experiments and collected and analyzed the data. Z. R., R. L., and Z. W. carried out the DFT calculations. C.M. and Y.X. carried out AC-HAADF-STEM test. Z.C., Z.S., and G.C. helped with data analysis. T.G. carried out the XAS experiment. W.J. and Z.C. wrote the manuscript with support from all authors.

Competing interests

The authors declare no competing interests.

Additional information

Supplementary information The online version contains supplementary material available at https://doi.org/10.1038/s41467-025-56240-y.

Correspondence and requests for materials should be addressed to Ziyun Wang or Yunhu Han.

Peer review information *Nature Communications* thanks Yong Xu, and the other, anonymous, reviewer(s) for their contribution to the peer review of this work. A peer review file is available.

Reprints and permissions information is available at http://www.nature.com/reprints